Wavelet Foveation

Ee-Chien Chang

Department of Computational Science,

National University of Singapore

Stéphane Mallat

Centre de Mathématiques Appliquées,

École Polytechnique and

Courant Institute of Mathematical Sciences,

New York University

Chee Yap

Courant Institute of Mathematical Sciences,

New York University

January 14, 1999

Abstract

A foveated image is a non-uniform resolution image whose resolution is highest at a point (fovea) but falls off away from the fovea. It can be obtained from a uniform image through a space-variant smoothing process, where the width of the smoothing function is small near the fovea and gradually expanding as the distance from the fovea increases. We treat this process as an integral operator and analyze its kernel. This kernel is dominated by its diagonal in the wavelet bases and thus permits a fast algorithm for foveating images. In addition, the transformed kernel takes a simple form which can be easily computed using a look-up table. This is useful since in applications, the fovea changes rapidly. We describe an application of our approximation algorithm in image visualization over the Internet.

1 Introduction

Figure 1(a) is a uniform resolution image whereas Figure 1(b) is a *foveated* image. A foveated image has non-uniform resolution. Its resolution is highest at the *fovea* but falls off as the distance from the fovea increases. We call the process of going from a uniform image to a foveated image *foveation*. A foveated image is obtained from a uniform resolution image through a space-variant smoothing process where the width of the smoothing function is small near the fovea but gradually increases towards the peripheral. In one dimension, the *foveation* of a function $f : \mathbb{R} \to \mathbb{R}$ is determined by a *smoothing function* $g : \mathbb{R} \to \mathbb{R}$, and a *weight function* $w : \mathbb{R} \to \mathbb{R}_{\geq 0}$.

$$(Tf)(x) := \int_{-\infty}^{\infty} f(t) \frac{1}{w(x)} g\left(\frac{t-x}{w(x)}\right) dt. \tag{1}$$

The weight w depends upon three parameters and takes the form $w(x) = \alpha|x-\gamma| + \beta$. We call α the *rate* as it determines how fast resolution falls off, call γ the fovea as it determines the point of highest resolution, and call

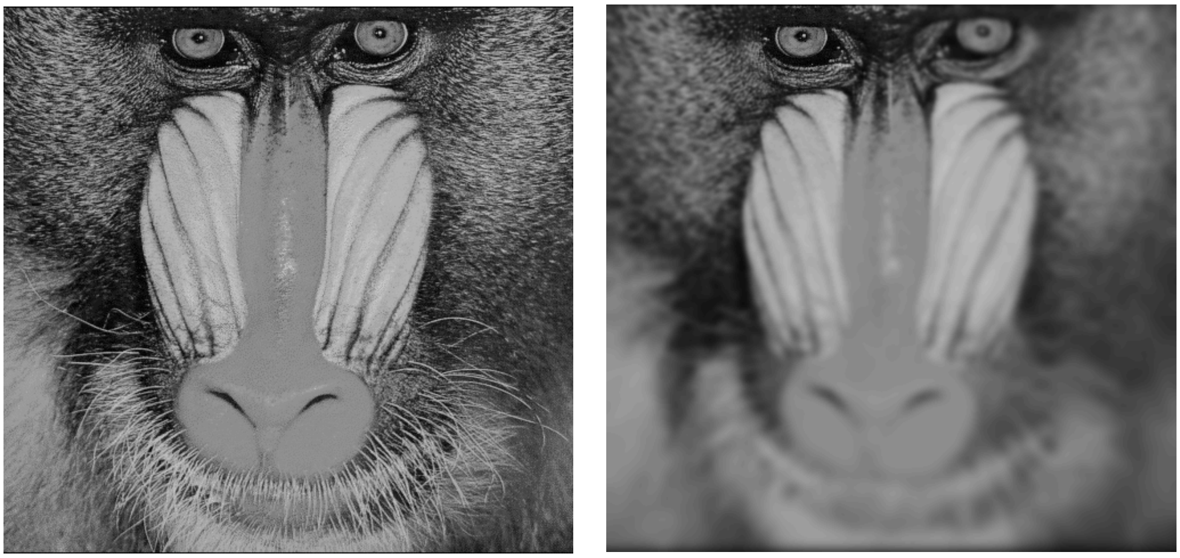

(a) Uniform resolution image. (b) Foveated image

Figure 1: Foveation.

β the *foveal resolution* as it determines the resolution at the fovea. Both α and β are non-negative. The smoothing function g is normalized so that $\int_{-\infty}^{\infty} g(x)\,dx = 1$. Figure 2 shows an example of a foveation with Gaussian as the smoothing function. In general, we could replace the weight function by any non-negative function. This generalization is useful when we are interested in images with multiple foveae. Similar formulations of foveation could be found in [9, 28].

The foveation operator can be treated as an integral operator

$$(Tf)(x) = \int_{-\infty}^{\infty} k(x,t) f(t)\,dt,$$

where $k(x,t)$ is the kernel of T. Wavelets of high vanishing moments have demonstrated their potential in approximating an integral operator [4], due to their ability to build sparse representation for piecewise smooth functions. In the foveation operator, the width of the function $k(\cdot, t_0)$ on x grows as the value of t_0 increases. Figure 3 is the contour plot of $k(x,t)$. Note

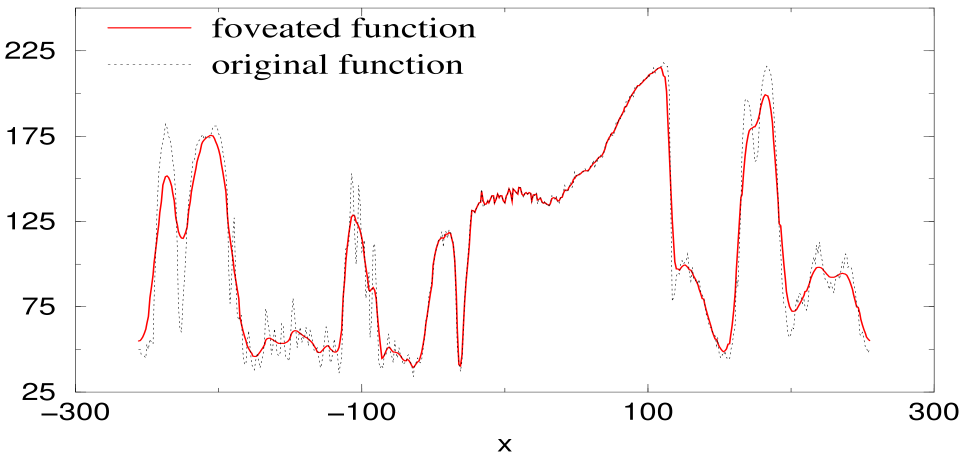

Figure 2: The dotted line is the original function f and the solid line is the corresponding foveated function Tf with weight function $w(x) = (1/45)|x|$. The fovea is at the origin. This function is a scan-line from the test image "Lena" (Figure 12(a)). Observe that details are retained near the fovea but gradually disappear as the distance from the fovea increases. The smoothing function g is the Gaussian.

that the kernel is smooth except at the origin. This paper shows that the wavelet decomposition of this kernel is dominated by its diagonal, and gives numerical results to support these findings.

Applications of foveation. Our visual system has a space-variant nature where the resolution is high in the center (fovea) but falls off toward the peripheral. This distribution of resolution provides a fast and simple way of reducing information in the visual field, without sacrificing the size of the visual field and the resolution around the center. As the biological visual system is highly effective, this space-variant nature has inspired the design of many computer vision systems. Under the framework of active vision [1, 27, 25], Burt introduces smart sensing [5] which resembles the bio-

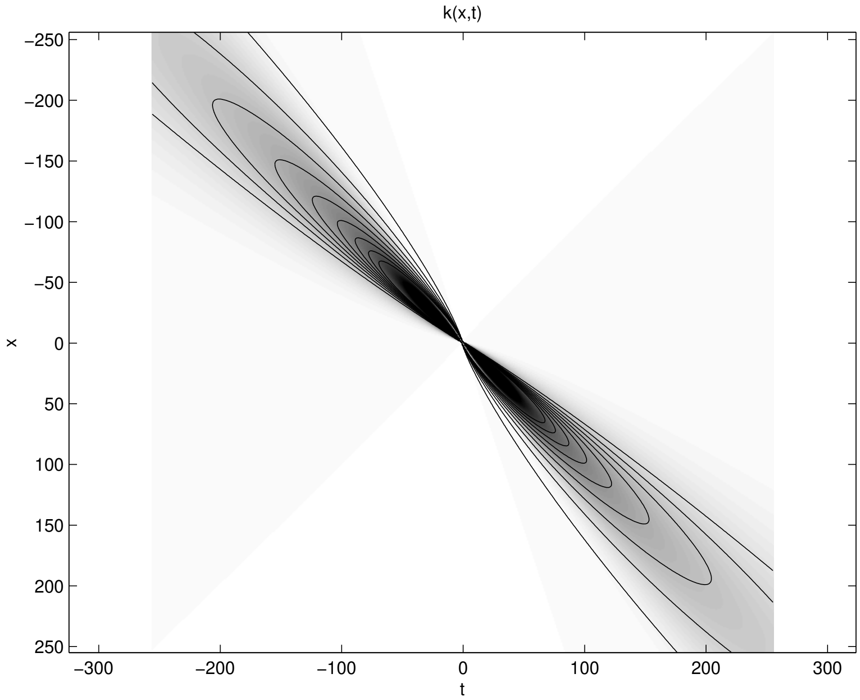

Figure 3: The kernel plotted as an image (darker pixel corresponds to a larger value) together with its contour plot. Observe that it is smooth except at the origin.

logical foveated vision. During the smart sensing process, the fovea actively and adaptively searches for interesting features; as a result, a sequence of foveated images are analyzed. We could view smart sensing as a hill climbing strategy which uses information across different scales.

The space-variant nature of our visual system suggests that if a viewer's gaze point is fixed at the fovea of a foveated image, the viewer could not distinguish this foveated image from the original uniform image. Since a foveated image carries much less information compared to the original uniform image, it can be encoded by fewer number of bytes. This observation has been exploited by visualization systems where transmission of images to the display device is a bottleneck, for example, in video conferencing [2, 3, 11]. Foveation also plays a role in visualization systems where the image rendering process is not fast enough to meet the real-time requirement, for example in volume visualization [16] and flight simulation [31, 12].

All the applications mentioned rely on the observation that information is reduced in a foveated image. Therefore, it is essential that the representations for foveated images capture this observation. To illustrate, in video conferencing, a foveated image should be encoded with significantly fewer bytes than the original uniform image. In most applications, the location and shape of the fovea changes rapidly. Thus, a fast algorithm is required to extract the foveated images from the original image.

A number of representations of foveated images have been proposed. In [15, 32], the visual field is partitioned into cells known as super-pixels. The value of a super-pixel is obtained by averaging all pixels in the corresponding cell. To construct a foveated image, the value of all pixels in a cell is replaced by the value of the super-pixel. These methods are computationally fast but lack flexibility in the sense that the visual field has to be repartitioned if the location and shape of the fovea changes. Another method by Burt [5] uses subband coding as a hierarchical representation of the original uniform image, and the foveated image is extracted from various levels. The third basic approach is based on the log-polar transformation [30, 28], where the foveated image is obtained by first transforming the visual field under a log-polar transformation, followed by a convolution and the inverse log-polar transformation.

In this paper, we derived a wavelet-based method for approximating the foveation operator (1). This method is computationally fast and can be extended for various weight functions. Furthermore, it permits progressive transmission (or progressive refinement) of images with multiple foveae.

Outline of this paper. Section 2 describes the relationship between the foveation operator and the space-variant nature of our visual system. The main results of this paper are in Section 3 which consists of a few subsections, starting with a brief introduction to wavelets in the first subsection. The second subsection studies the operator using wavelet and show that under the wavelet representation, the transformed kernel is dominated by the diagonal entries. The supporting numerical results are shown in the third subsection. In the fourth subsection, we give an approximation of the diagonal entries (of the transformed kernel), which gives good numerically approximation and provides insight on the roles of the wavelet. The last subsection gives an approximation of the operator obtained by suppressing small values in the transformed kernel. Section 4 generalizes foveation to two dimensions. Finally, Section 5 describes applications of foveation in image compression and image visualization over the Internet.

2 Logmap and Foveation Operator

Studies of the space-variant structure in the visual cortex could be traced back to the papers [20, 14, 23], who suggest a well-defined map-like representation of the visual field in the cortex. In the early 1940s, Talbot and Marshall [29] demonstrated and confirmed this hypothesis. Subsequent studies by Schwartz [24] show that the complex logmap is a good model for this mapping. The logmap (or log-polar map) is characterized by two real parameters k, a and maps the point (x, y) in the *retinal plane* to a point (ρ, θ) in the *visual cortex plane* where

$$\begin{aligned} \rho &:= k \ln(\sqrt{(|x|+a)^2 + y^2}), \quad \text{and} \\ \theta &:= \begin{cases} \tan^{-1}\left(\frac{y}{x+a}\right) & \text{if } x > 0, \\ \tan^{-1}\left(\frac{y}{x-a}\right) + \pi & \text{otherwise.} \end{cases} \end{aligned} \tag{2}$$

For engineering purposes, it is not necessary to adhere to the logmap (2). Thus, we use the term "logmap" loosely and use it to refer to transformations that have the log-polar favor. Other forms of logmap can be found in [22, 21]. Schwartz [26] has an overview of the biological background.

Our definitions of foveation operators and weight functions are motivated by the logmap, which attempt to capture the situation in which convolution is performed in the visual cortex plane. Consider a function f where $f(t) = 0$ for $t < 0$. We could rewrite foveation as a convolution after a change of variables. For $x > 0$,

$$\begin{aligned} (Tf)(x) &= \int_0^\infty f(t) \frac{1}{x} g\left(\frac{t-x}{x}\right) dt \\ &= \int_0^\infty f(e^u) e^{-y} g\left(\frac{e^u - e^y}{e^y}\right) de^u \\ &\quad \text{(where } e^y = x \text{ and } e^u = t) \\ &= \left(\tilde{f} \star \tilde{g}\right)(y), \end{aligned} \tag{3}$$

where

$$\begin{aligned} \tilde{f}(u) &:= f(e^u), \text{ and} \\ \tilde{g}(v) &:= e^{-v} g\left(e^{-v} - 1\right). \end{aligned}$$

Equation (3) suggests a method to compute foveation: apply the logmap transform, followed by a convolution and the inverse logmap transform [28].

To ensure that the computations are stable, it is important to show that T is a bounded operator. Since the operator can be treated as a convolution after a logmap transformation, one would expect this to be the case. We can show the boundedness along this intuition. We state the following theorem and give the proof in the Appendix.

Theorem 1 *Let g be bounded and $g \in L^1(\mathbb{R})$. The operator*

$$(Tf)(x) = \int_{-\infty}^{\infty} f(t) \frac{1}{|x|} g\left(\frac{t-x}{|x|}\right) dt$$

is bounded in L^2 and

$$\|T\| \leq \int_{-\infty}^{\infty} (|g(u-1)| + |g(u+1)|) \frac{du}{\sqrt{u}} < \infty.$$

3 Wavelet and Foveation Operator

Recall that

$$(Tf)(x) = \int_{-\infty}^{\infty} k(x,t) f(t)\, dt,$$

where $k(x,t) = |x|^{-1} g((t-x)/|x|)$. If we take N sample points from f uniformly, then computation of the foveated function amounts to a matrix multiplication, which takes $O(N^2)$ arithmetic operations. For some integral operators, by representing the kernel using a wavelet base, the magnitude of most entries in the transformed kernel become small. Suppressing these small entries gives a sparse matrix. Together with the fast wavelet transform, this sparse matrix provides a fast approximation for the integral operator which could take $O(N)$ arithmetic operations. In this section, we show that a fast approximation for the foveation operator can be similarly obtained.

3.1 Wavelet Bases

Wavelet bases have important applications in mathematics and signal processing due to their ability to build sparse representations for large classes of functions. The first orthonormal wavelet bases were introduced by Strömberg and Meyer [19]. A multi-resolution interpretation of wavelet bases provides a general framework for constructing wavelets [17]. It also leads to a fast discrete algorithm that takes $O(N)$ arithmetic operations to compute N wavelet coefficients [18]. Daubechies [10] discovered wavelets with compact support. An orthonormal wavelet base of $L^2[0,1]$ is a family of functions

$$\{\phi_{\ell_0,n}\}_{0\leq n<2^{\ell_0}} \cup \{\psi_{j,n}\}_{j\leq \ell_0, 0\leq n<2^{-j}}.$$

Each $\psi_{j,n}$ is a dilated and translated copy of the *mother* wavelet ψ,

$$\psi_{j,n}(t) = \sqrt{2^{-j}}\psi\left(2^{-j}t - n\right),$$

and each $\phi_{\ell_0,n}$ is a dilated and translated copy of the *scaling* function ϕ,

$$\phi_{\ell_0,n}(t) = \sqrt{2^{-\ell_0}}\phi\left(2^{-\ell_0}t - n\right).$$

The subspace V_ℓ at scale ℓ is the subspace generated by

$$\{\phi_{\ell_0,n}\}_{0\leq n<2^{\ell_0}} \cup \{\psi_{j,n}\}_{\ell<j\leq \ell_0, 0\leq n<2^{j}}.$$

Boundary wavelets are modified to keep the support inside $[0,1]$.

The subspaces at different scales $V_{\ell_0} \subset V_{\ell_0-1} \subset V_{\ell_0-2} \subset \ldots$ form a multi-resolution ladder: each V_ℓ is coarser than $V_{\ell-1}$. The approximation of a function f at scale ℓ is

$$\sum_{0\leq n<2^{\ell_0}} \langle f, \phi_{\ell_0,n}\rangle \phi_{\ell_0,n} + \sum_{\ell<j\leq\ell_0} \sum_{0\leq n<2^j} \langle f, \psi_{j,n}\rangle \psi_{j,n}.$$

The wavelet coefficients $\{\langle f, \psi_{j,m}\rangle\}_{j,m}$ of a function f are small in the finer scale (smaller j) and in the neighborhood where f is smooth. Thus, in finer scale, the above approximation contains more local "details." By truncating the small coefficients, we have an adaptive sparse representation of f.

In two dimensions, the ladder is constructed using three mother wavelets, $\Psi^{\mathrm{h}}, \Psi^{\mathrm{v}}$ and Ψ^{d}, where

$$\Psi^{\mathrm{d}}_{j,m,n}(x,y) \quad := \quad \psi_{j,m}(x)\psi_{j,n}(y),$$

$$\begin{aligned}\Psi^{\mathrm{v}}_{j,m,n}(x,y) &:= \psi_{j,m}(x)\phi_{j,n}(y), \quad \text{and} \\ \Psi^{\mathrm{h}}_{j,m,n}(x,y) &:= \phi_{j,m}(x)\psi_{j,n}(y),\end{aligned}$$

with the scaling function

$$\Phi_{j,m,n}(x,y) := \phi_{j,m}(x)\phi_{j,n}(y).$$

The wavelet coefficients for $\{\Psi^k_{j,m,n}\}$, $k \in \{\mathrm{h},\mathrm{v},\mathrm{d}\}$, are sensitive to the local orientation of edges in the images and are interpreted as the horizontal, vertical, and diagonal components respectively. Figure 4 shows an example of a wavelet transform. Note that most of the coefficients are small except in the neighborhood of an edge. Also note how the local orientation of an edge affects the coefficients in different components.

3.2 Analytic Bounds

Consider a foveation operator T with a weight function $w(x) = \alpha|x|$, and a smoothing function g whose support is in $[-\alpha^{-1}, \alpha^{-1}]$. Let

$$\begin{aligned}\theta_{j,m,k,n} &:= \langle T\psi_{j,m}, \psi_{k,n}\rangle \qquad (4)\\ &= \int_{-\infty}^{\infty}\int_{-\infty}^{\infty} \psi_{j,m}(t)\psi_{k,n}(x)\frac{1}{\alpha|x|} g\left(\frac{t-x}{\alpha|x|}\right) dt\, dx.\end{aligned}$$

The matrix $\{\theta_{j,m,k,n}\}$ can be viewed as the wavelet transform of the kernel along the t-axis followed by wavelet transform along the x-axis.

It is easy to verify the following property.

Property 2 (Self-Similarity)

$$\theta_{j,m,k,n} = \theta_{j-\ell,m,k-\ell,n} \quad \textit{for any} \;\; \ell \in \mathbb{Z}.$$

Intuitively, this property tells us that the amount of information stored in a foveated image is the same across different scales.

The next two theorems show the decays in the matrix $\{\theta_{j,m,k,n}\}$. These results are derived by exploiting the number of vanishing moments ψ has

(a) (b)

Figure 4: (a) Original image I. (b) Magnitude of coefficient for $\{|\langle I, \Psi^k_{j,m,n}\rangle|\}_{j,m,n}$. The bottom right square contains the diagonal coefficients for $\{\Psi^{\mathrm{d}}_{0,m,n}\}_{m,n}$, the upper right square contains the vertical coefficients for $\{\Psi^{\mathrm{v}}_{0,m,n}\}_{m,n}$ and the bottom left square contains the horizontal coefficients for $\{\Psi^{\mathrm{h}}_{0,m,n}\}_{m,n}$. Coefficients in higher scales (smaller j) are recursively arranged in the upper left square.

and by using the fact that both ψ and g have compact support. We state the theorems and explain their implications on the decay. Their proofs are rather technical and we describe them in the Appendix.

Theorem 3 *Suppose the support of both ψ and g is compact and contained in $[-\alpha^{-1}, \alpha^{-1}]$, ψ is C^p, and ψ has p vanishing moments; then we have the following.*

(a) There is a constant J such that for any j, k, n and m,

$$|\theta_{j,m,k,n}| \quad \leq \quad J 2^{-|k-j|/2}.$$

(b) For $|n| > 2\alpha^{-1}$ and $|m| > 2\alpha^{-1}$, if $\theta_{j,m,k,n} \neq 0$, then

$$C|m| > 2^{k-j}|n| > C^{-1}|m|,$$

where C is a constant.

(c) There is a constant E such that for any j, m, k, n, when either $|n| > 2\alpha^{-1}$ or $|m| > 2\alpha^{-1}$, we have

$$|\theta_{j,m,k,n}| \quad \leq \quad E\ 2^{-|k-j|(p+1/2)}.$$

Using the fact that both ψ and g have compact support, we have part (a) and (b) in Theorem 3. Part (a) tells us that $\theta_{j,m,k,n}$ is small if $|k-j|$ is large while part (b) states that for $\theta_{j,m,k,n}$ to be non-zero, m is on the order of $2^{k-j}n$. Together, they imply a decay off the diagonal. The third part (c) gives a sharper bound than part (a); however it is only applicable for large $|m|$ or large $|n|$. Note that the decay in (c) depends on the regularity and the vanishing moments of the wavelet.

Theorem 4 *Suppose the support of both ψ and g is compact and contained in $[-\alpha^{-1}, \alpha^{-1}]$, and ψ is C^p and has p vanishing moments; if g is uniformly*

Lipschitz $\rho < p$, then for any $|n| > 2\alpha^{-1}, |m| > 2\alpha^{-1}$ and any j, k, there is a constant F such that

$$\begin{aligned} |\theta_{j,m,k,n}| &\leq F\ 2^{(j-k)(\rho+1/2)}|n|^{-(\rho+1)}, \quad \textit{and} \\ |\theta_{j,m,k,n}| &\leq F\ 2^{-(j-k)/2}|m|^{-(\rho+1)}. \end{aligned}$$

Theorem 4 suggests a relatively slower decay away from the fovea. It gives a bound that decays as $|m|$ or $|n|$ increase and relates the rate of decay to the regularity of the smoothing function g.

In sum, the matrix $\{\theta_{j,m,k,n}\}$ decays in two directions: off the diagonal, $\{\theta_{j,m,k,n}\}$ decays as $|k-j|$ and $|m-n|$ increases; while along the diagonal, $\{\theta_{j,m,j,m}\}$ decays as $|m|$ increases.

3.3 Numerical Results

Let us compute, numerically, the matrix $\{\theta_{j,m,k,n}\}$. Figure 5 illustrates such a matrix computed using the Daubechies wavelet with four vanishing moments [10]. The smoothing function is the Gaussian and the weight function is $w(x) = |x|/30$. A quick visual inspection suggests that the matrix is dominated by the diagonal entries $\theta_{j,m,j,m}$ where $j, m \in \mathbb{Z}$. In addition, the diagonal entries decay relatively slower away from the fovea. This decay along the diagonal is easily observed in the cross-section plot shown in Figure 6. Another observation from Figure 6 is the self similarity across the scales, that is, $\theta_{j,n,j,n} = \theta_{k,n,k,n}$ for any n, j, and k.

3.4 Approximating the Diagonal

Although the analytic bounds are sufficient to show the decays in the transformed kernel, the predicted decays are still far from the numerical results observed. Here, we give an approximation of the diagonal $\{\theta_{j,n,j,n}\}$ which, besides being a good approximation, also gives more insights on the roles of ψ and g.

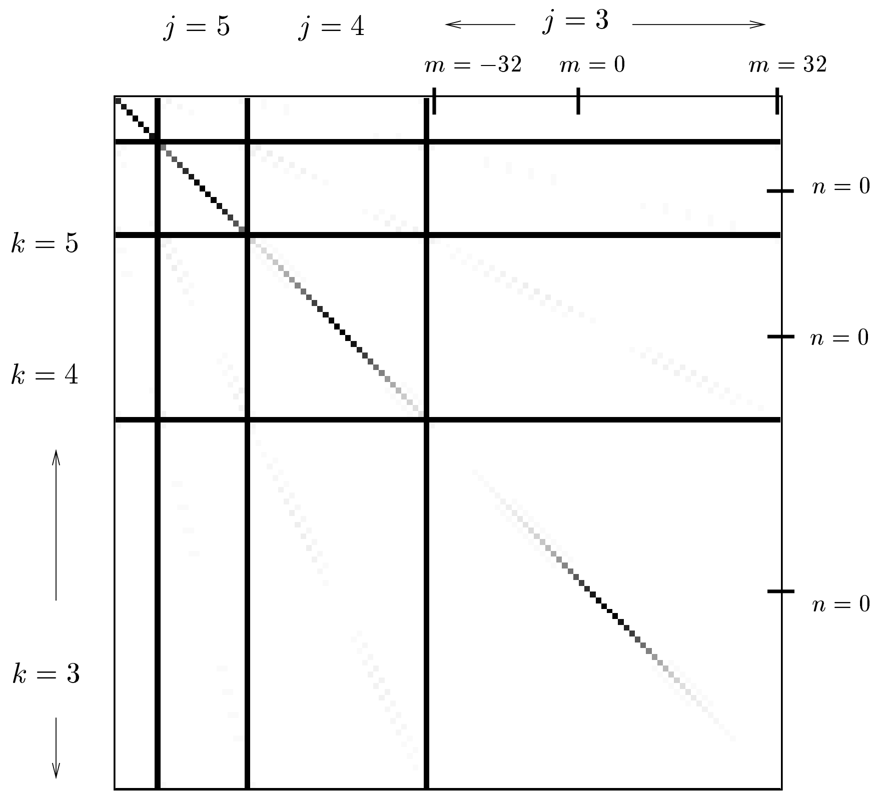

Figure 5: Computed numerical value of the matrix $\{\theta_{j,m,k,n}\}$. The entries are grouped into blocks where each block consists of entries with the same first and third index. For example, the block in the top-right corner consists of entries of the form $\theta_{3,m,6,n}$ where $-32 \leq m \leq 32$ and $-4 \leq n \leq 4$. The intensity of each pixel corresponds to the value of the corresponding entry; a darker pixel has a larger value.

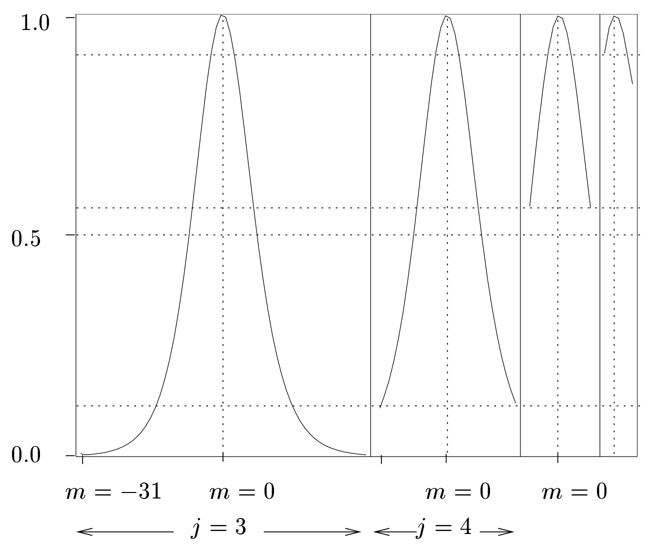

Figure 6: The cross-section of Figure 5 along the diagonal $\theta_{j,m,j,m}$. Note the decays and the self-similarity across different scales.

By the compact support of ψ,

$$\theta_{0,n,0,n} = \int_{n-A}^{n+A} \int_{-\infty}^{\infty} \psi_{0,n}(x)\psi_{0,n}(t)g_x(t)\,dt\,dx,$$

where $g_x(t) := (\alpha|x|)^{-1} g\left((\alpha|x|)^{-1}(t-x)\right)$, and A is a constant. For large positive n, $h_n(\cdot - x)$ is a good approximation of g_x, where

$$h_n(t) := \frac{1}{\alpha n} g\left(\frac{t}{\alpha n}\right).$$

Using this approximation, we have a much simpler form:

$$c_n := \int_{-\infty}^{\infty} \int_{-\infty}^{\infty} \psi_{0,n}(x)h_n(t-x)\psi_{0,n}(t)\,dt\,dx. \tag{5}$$

Figure 7 shows that the absolute error is below 0.02.

Equation (5) can be further simplified. By interchanging the integrals (which is possible by Fubini's theorem) and treating the first two terms as a convolution, it can be rewritten as:

$$c_n = \int_{-\infty}^{\infty} (\psi_{0,n} \star h_n)(t)\psi_{0,n}(t)\,dt.$$

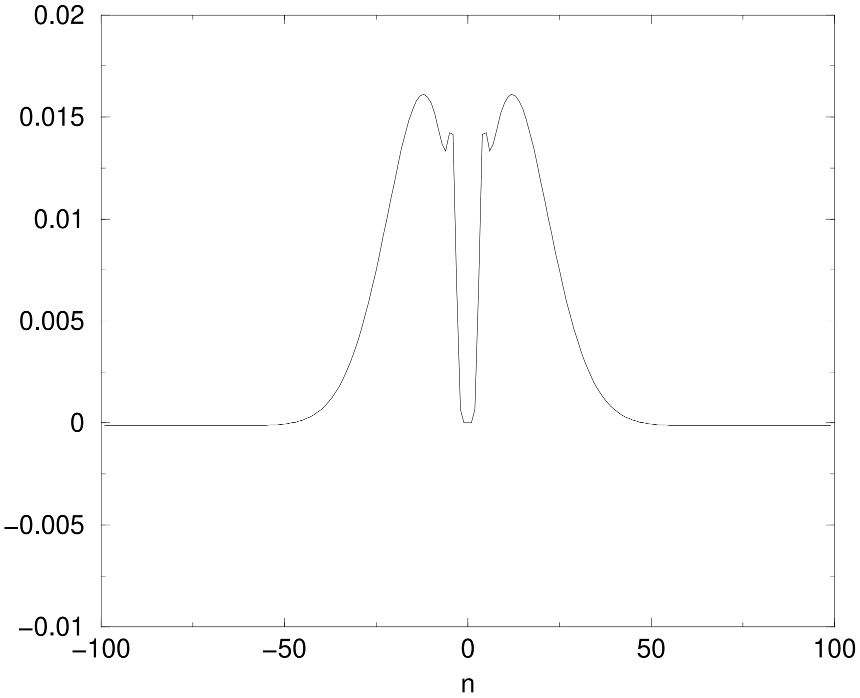

Figure 7: The absolute error in approximation $\{\theta_{j_0,n,j_0,n}\}$ using (5). This graph is computed by evaluating the numerical difference between approximation (5) and the results in Figure 6.

By applying Parseval's formula and the convolution theorem, we have

$$|c_n| \quad = \quad \int_{-\infty}^{\infty} \overline{\widehat{g}\left((\alpha n)w\right)} \left|\widehat{\psi}(w)\right|^2 \, dw.$$

Since ψ has compact support, $\hat{\psi}$ is at least p times continuously differentiable. Together with the fact that ψ has p vanishing moments, we have $\hat{\psi}^{(k)}(0) = 0$ for $k < p$. Thus, $|\hat{\psi}(w)| \le Cw^p$ for some constant C, and

$$\begin{aligned} |c_n| &\le C^2 \int_{-\infty}^{\infty} \left|\hat{g}\left((\alpha n)w\right)\right| w^{2p} \, dw \\ &= C^2 (\alpha n)^{-2p-1} \int_{-\infty}^{\infty} |\hat{g}(w)| \, w^{2p} \, dw. \end{aligned}$$

Furthermore, as g is at least $2p$ times continuously differentiable, we have

$$\int_{-\infty}^{\infty} |\hat{g}(w)| \, |w|^{2p} < \infty,$$

and this gives $|c_n| = O((\alpha n)^{-2p-1})$. This bound is tighter than the bounds given by Theorem 4.

Similarly, the following is a good approximation of $\langle T\phi, \phi\rangle$.

$$e_n := \int_{-\infty}^{\infty} \overline{\widehat{h}_n(w)} \left|\widehat{\phi}(w)\right|^2 \, dw.$$

Since $|\hat{\phi}(0)| = 1$, we expect a slower decay:

$$\begin{aligned} e_n &\le E \int_{-\infty}^{\infty} |\hat{h}_n(w)| \, dw \\ &= \frac{E}{\alpha n} \int_{-\infty}^{\infty} |\hat{g}(w)| \, dw = E_1 (\alpha n)^{-1}, \\ &\qquad \text{where } E \text{ and } E_1 \text{ are some constants.} \end{aligned}$$

The effect of this slower decay appears in two dimensional foveation, and we will revisit this in Section 3.5.

3.5 Approximation of Foveation

Given the $N = 2^{\ell_0}$ uniform samples of a function f, we want to compute Tf. Since the kernel (with respect to a wavelet ψ) is dominated by the diagonal, suppressing all entries off the diagonal, we have the following approximation of Tf.

$$Tf \approx \langle f, \phi_{\ell_0,0} \rangle \phi_{\ell_0,0} + \sum_{j=1}^{\ell_0} \sum_{n=0}^{2^j-1} \theta_{j,n,j,n} d_j[n] \psi_{j,n}, \tag{6}$$

where each $d_j[n] := \langle f, \psi_{j,n} \rangle$. In the above approximation, we ignore the boundary effect and approximate $\langle T\phi_{\ell_0,0}, \phi_{\ell_0,0} \rangle$ by 1. The wavelet coefficient $\{d_j[n]\}_{j,n}$ can be computed from the uniform sample of f using the linear time fast wavelet transform. Conversely, the double summation can be computed in linear time using the fast inverse wavelet transform. Thus, given a function represented by its uniform sample points, we can compute its foveated image in linear time, provided that the diagonal $\{\theta_{j,n,j,n}\}$ is precomputed. Let us call the precomputed diagonal $\{\theta_{j,n,j,n}\}$ the *mask*.

The mask could be precomputed directly from its definition or from the approximation (5). Figure 8 shows the computed mask which is plotted as functions of n for different j. Note that it contradicts self-similarity (Property 2). This is due to the error induced in sampling the kernel and f. (In Figure 6, the values are computed in high resolution; thus the self-similarity property is retained). In coarser scale, the kernel for $j > 3$ are well approximated by $j = 3$. In Figure 8, the diagonal $\{\theta_{j,n,j,n}\}$ for $j > 3$ is not shown as it overlaps with the entries at $j = 3$.

Figure 9(a) is an approximation of a foveated function using (6). The error of this approximation is shown in Figure 10(c).

Look-up table. The above approximation assumes that the weight function takes the form $w(x) = \alpha|x|$. For weight functions with non-zero fovea γ and foveal resolution β, we can similarly show the decays in the corresponding transformed kernel. Thus, similar approximation can be extended to this class of weight functions.

In most applications, the parameters α, γ, and β change rapidly. Thus,

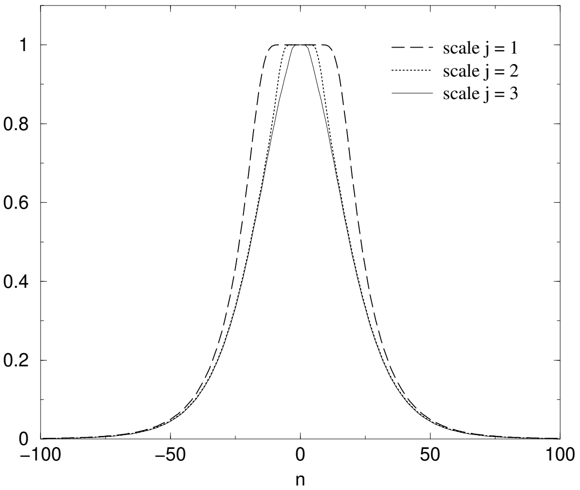

Figure 8: The entries $\theta_{j,n,j,n}$ computed numerically. The samples are taken uniformly at a unit spacing.

it is important to compute the corresponding diagonal $\{\theta_{j,n,j,n}\}$ efficiently. A fast and simple approximation can be achieved by a "look-up" procedure which uses a table L of size L_{size}. The entries in L are the diagonal with respect to a weight function

$$w_0(x) := \alpha_0 |x|,$$

where α_0 is some small constant. Typically, a good choice of α_0 is $(L_{\text{size}})^{-1}$. The mask corresponding to different weight functions are looked up from this table. Let us define $\{\theta_{j,n}^{\alpha,\beta}\}$ to be the diagonal corresponding to the foveation whose weight function is $w(x) = \alpha|x| + \beta$. To approximate $\theta_{j,n}^{\alpha,\beta}$, the look-up procedure returns $L[k]$ where

$$k := \left\lfloor \frac{\alpha}{\alpha_0}(|n| + 2^{-j}\beta) \right\rfloor .$$

If $(k > L_{\text{size}})$, then the value zero is returned.

In particular, if $\beta = 0$ but $\alpha \neq \alpha_0$, then the look-up amounts to a dilation of the table by a factor of α. If $\alpha = \alpha_0$ but $\beta \neq 0$, then the look-up amounts to a translation. When γ is non-zero, we could approximate the diagonal by shifting the look-up table. This look-up procedure can be justified by using a similar trick in deriving (5).

A simplified approximation. An interesting simplification is by further approximating each diagonal entry $\theta_{j,n,j,n}$ by it's rounded value $\mathrm{ROUND}_D(\theta_{j,n,j,n})$, where

$$\mathrm{ROUND}_D(x) = \begin{cases} 1 & \text{if } x > D, \text{ and} \\ 0 & \text{otherwise,} \end{cases} \tag{7}$$

for some constant D. Call this simplified mask the *0-1 mask*.

This method of using a 0-1 mask to produce a foveated image is essentially the technique of Burt [5]. In a certain sense, we give a justification of this technique by arguing that it is indeed an approximation of the foveation operator. Figure 9(b) shows the approximation of a foveated function using a 0-1 mask and Figure 10 compares the error in using the diagonal and a 0-1 mask.

The advantages of the 0-1 mask are simplicity and computational speedup in the reconstruction process. An example is volume rendering [6], where the projection of the volume data onto a plane is computed by performing a texture mapping operation for each non-zero coefficient.

4 Generalization to two dimension

Most applications of foveation are for two dimensional images. Given a two dimensional image I, its foveation is determined by a smoothing function g and a weight function w.

$$(TI)\,(x,y) := \langle I, g_{x,y} \rangle. \tag{8}$$

Each $g_{x,y}$ is the translated and dilated version of the smoothing g. Its center is translated to (x,y) and its width is dilated by a factor of $w(x,y)$.

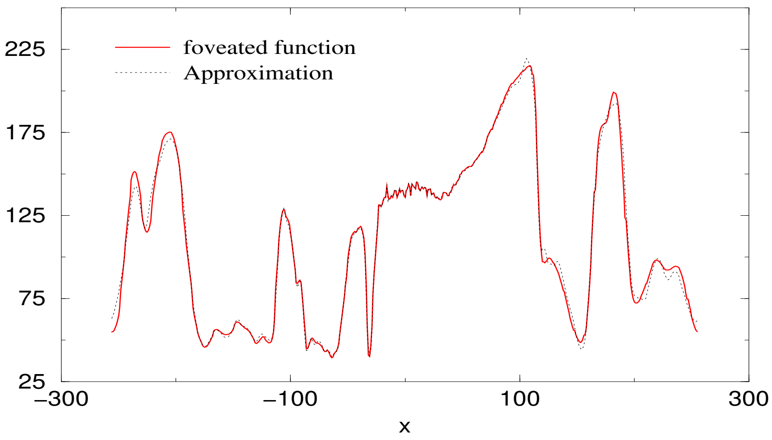

(a)

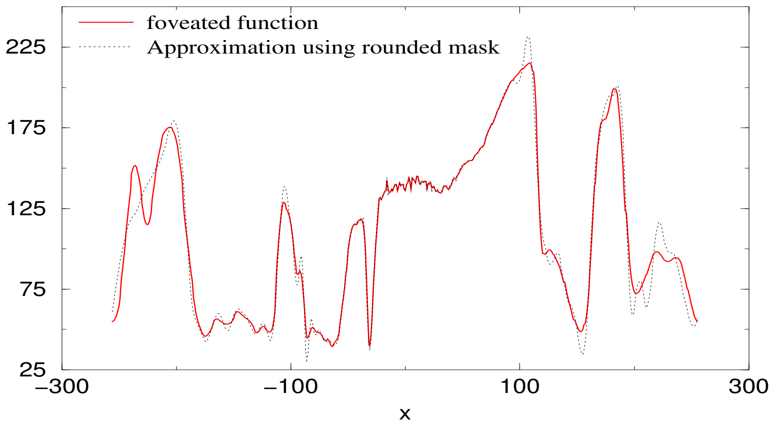

(b)

Figure 9: (a) The darker line is the foveated f as in Figure 2. The lighter line is an approximation computed using only the diagonal in the operation matrix. (b) Same as (a) except that each diagonal entry is rounded to 0 or 1.

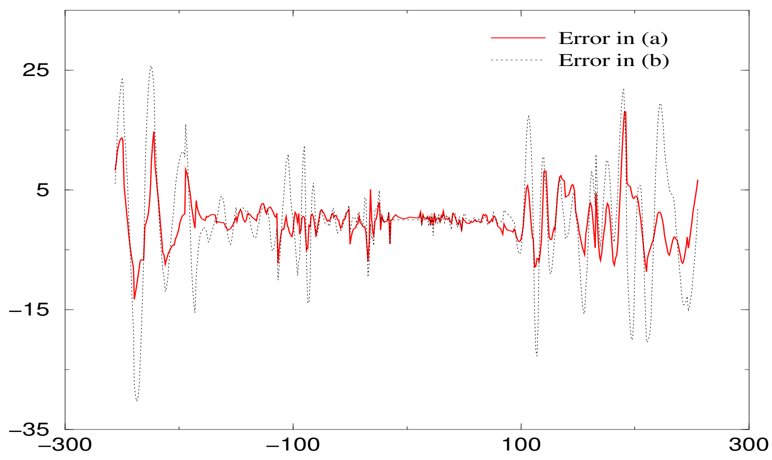

Figure 10: The solid and dotted line is the error in Figure 9(a) and 9(b) respectively. The error in (b) is clearly larger than that in (a).

In addition, each $g_{x,y}$ is normalized under 1-norm. Specifically,

$$g_{x,y}(s,t) := \frac{1}{w(x,y)^2} g\left(\frac{s-x}{w(x,y)}, \frac{t-y}{w(x,y)}\right).$$

In two dimensions, the weight function takes the form $w(x,y) = \alpha\|(x,y) - (\gamma_1, \gamma_2)\|_2 + \beta$, where α, $\gamma = (\gamma_1, \gamma_2)$ and β are the rate, fovea, and foveal resolution respectively. Figure 12(b) is the foveated image of Figure 12(a).

Similar to the one-dimensional case, in two dimensions, we transform the kernel using a wavelet. By choosing a compactly supported smoothing function and a wavelet, it is easy (but tedious) to show an off-diagonal decay in the transformed kernel. Along the diagonal, for a separable smoothing function and suitable wavelet, we can show a decay away from the fovea. We omit the details.

To see the different roles of the three mother wavelets Ψ^k where $k \in \{\mathrm{h}, \mathrm{v}, \mathrm{d}\}$, let us consider an approximation. Let $\{c_j^k[m,n]\}$ be the diagonal entries:

$$c_j^k[m,n] = \left\langle T\Psi^k_{0,m,n}, \Psi^k_{0,m,n}\right\rangle$$

$$= \int_{-\infty}^{\infty} dy \int_{-\infty}^{\infty} dx \ \Psi_{0,m,n}^{k}(x,y) \int_{-\infty}^{\infty} dt \int_{-\infty}^{\infty} ds \ \Psi_{0,m,n}^{k}(s,t) g_{w(x,y)}(s,t).$$

Note that the support of Ψ^k is in the domain $[m - A, m + A] \times [n - A, n + A]$, where A is some constant. For large m or n, we can approximate $w(x,y)$ by the constant $w(m,n)$. Thus, if g is separable, the function $g_{w(x,n)}(s) g_{w(m,y)}(t)$ is a good approximation of $g_{w(x,y)}(s,t)$. This simpler form gives the following approximation.

$$c_j^k[m,n] \approx \begin{cases} c_j[w(m,n)] \cdot b_j[w(m,n)], & \text{if } k = \text{v}, \\ b_j[w(m,n)] \cdot c_j[w(m,n)], & \text{if } k = \text{h}, \\ c_j[w(m,n)] \cdot c_j[w(m,n)], & \text{otherwise}, \end{cases}$$

where

$$\begin{aligned} c_j[r] &= \langle \psi_{j,r}, T(\psi_{j,r}) \rangle, \\ b_j[r] &= \langle \phi_{j,r}, T(\phi_{j,r}) \rangle, \text{ and } \ r = \|(m,n)\|_2. \end{aligned}$$

Recall that in Section 3.4, $\langle \phi_{j,m}, T(\phi_{j,m}) \rangle$ decays much slower than $\langle \psi_{j,m}, T(\psi_{j,m}) \rangle$. Thus the vertical component has a slower decay compared to the diagonal component.

Figure 11(a) shows the contour plot of $\{c_j^k[m,n]\}$. This two-dimensional contour plot is the diagonal entries of the four-dimensional transformed kernel. Figure 11(b) is the rounded version of Figure 11(a) using equation (7). A faster decay is observed in the diagonal component.

For an image I, its foveation can be approximated by

$$\langle I, \Phi_{\ell_0,0,0} \rangle + \sum_{k,m,n,j} c_j^k[m,n] \langle I, \Psi_{j,m,n}^k \rangle \Psi_{j,m,n}^k. \tag{9}$$

The wavelet coefficient $\{\langle I, \Psi_{j,m,n}^k \rangle\}$ can be obtained from the uniform sample of I using the linear time fast wavelet transform. Conversely, the summation in (9) can be computed in linear time using the fast inverse wavelet transform.

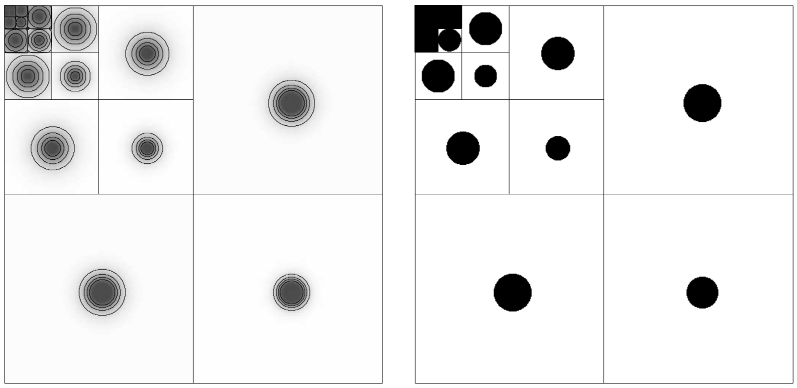

(a) (b)

Figure 11: (a)The contour plot $\{c_j^k[m,n]\}$. Note that the vertical component and diagonal component are different. (b) The simplified 0-1 Mask. The dark regions contain coefficients of value 1. The constant for the rounding function ROUND_D is $D = 0.4$.

Figure 12(c) is an approximation of Figure 12(b) obtained using (9) whereas Figure 12(d) is the approximation using the rounded 0-1 mask. The visual effect of using the 0-1 mask is an enhancement of the Gibbs phenomena along edges. This can be observed in Figure 12, especially along the edge of the "mirror."

5 Applications

Image Compression. Suppose we have prior knowledge of the viewer's point of interest in an image, we could achieve a higher compression rate by compressing the foveated image instead of the uniform image. The compressed foveated image is obtained by applying the existing compression scheme on the coefficients obtained by our approximation method.

To illustrate the compression rate, both Figure 12 (c) and (d) are re-

(a)

(b)

(c)

(d)

Figure 12: (a) Original image. (b) Foveation with foveal at her right eye and with rate $\alpha = 1/(80 \text{ pixels})$. (c) Computed using the mask as shown in Figure 11(a). (d) Computed using the 0-1 mask as shown in Figure 11(b).

constructed after the wavelet coefficients are quantized (that is rounded). After quantization, the number of non-zero coefficients required for (c) and (d) reduces to 7471 and 7460 respectively, which are both about 2.8 percent of the total number of coefficients required for the original image. Note that the performance of a compression scheme at high bit rate is essentially proportional to the number of non-zero coefficients [18].

Image Visualization. A number of previous works [15, 32] have indicated the potential of foveation in image visualization across the computer network. This idea could be enhanced by including progressive transmissions of a multi-foveated image (an image with more than one fovea) and allowing the viewer to interactively select the foveae [8, 13].

First, let us give a generalization of weight function to more than one fovea. We can obtain new weight function by combining several weight functions. Given two weight functions, their blended weight function w is defined as

$$w(x,y) = \min\{w_1(x,y), w_2(x,y)\}.$$

We call a weight function blended from several single-fovea weight functions a *multi-fovea* weight function. The foveated images with these weight functions may contain more than one fovea.

In our application of image visualization, a very large image is stored in the server and the viewer is connected to the server through the computer network. Both the server and viewer keep a multi-fovea weight function w_t, which changes as the time t increases. The task of the server is to provide the viewer the multi-foveated image with weight function w_t. The viewer could interactively modify w_t by blending w_t with another multi-fovea weight function w'. Note that this application is directed to images of very large size (possibly 5000 by 5000 pixels), and the viewer is only interested in a small and highly selective region of interests.

To send a multi-foveated image, the server computes its approximation using methods described in Section 3.5. Recall that this amounts to the pairwise multiplications between entries in the mask and the wavelet coefficients (of the original image). The coefficients of the approximated multi-foveated image are then quantized to some fixed precision. Next, these quantized coefficients are treated as bytes and sent across the network. The server keeps a history of what had been sent; thus it is not necessary to send all the bytes. Instead, the server could just send the additional bytes required for the multi-foveated image. This process iterates until the viewer stops the transmission.

A simplified version of this scheme is implemented in [7].

6 Conclusion

The idea of using wavelets in foveation has been investigated in many previous works. Non-wavelet method based on log-polar transformations and superpixel geometry have also been studied. Our novel approach amounts to first defining a mathematical foveation operator, and then giving a practical wavelet-based approximation to this operator. Our method is simple and flexible for multiple foveae, and is provably accurate (relative to the mathematical operator). It also permits progressive transmission of multi-foveated image. We have demonstrated the utility of our approach in two applications, namely visualization and image compression.

References

[1] J. Aloimonos, I. Weiss, and A. Bandyopadhyay. Active vision. In *1st International Conference on Computer Vision (London, England)*, pages 35–54, 1987.

[2] A. Basu, A. Sullivan, and K.J. Wiebe. Variable resolution teleconferencing. In *IEEE Systems, Man, and Cybernetics Conference*, pages 170–175, 1993.

[3] A. Basu and K.J. Wiebe. Videoconferencing using spatially varying sensing with multiple and moving fovea. *IEEE Trans. on Systems, Man and Cybernetics*, 28(2):137–148, 1998.

[4] G. Beylkin, R. Coifman, and V. Rokhlin. Wavelets in numerical analysis. In *Wavelets and Their Applications*, pages 181–210. Jones and Bartlett, 1992.

[5] P.J. Burt. Smart sensing within a pyramid vision machine. *Proceedings of the IEEE*, 76(8):1006–1015, 1988.

[6] B. Cabral, N. Cam, and J. Foran. Accelerated volume rendering and tomographic reconstruction using texture mapping hardware. *1994 Symp. on Volume Visualization*, pages 91–97, 1994.

[7] E.C. Chang. *Foveation Techniques and Scheduling Issues in Thinwire Visualization*. PhD thesis, Computer Science, Courant Institute, New York University, 1998.

[8] E.C. Chang, C.Yap, and T.J. Yen. Realtime visualization of large images over a thinwire. *IEEE Visualization 97 (late hot topics)*, 1997.

[9] E.C. Chang and C. Yap. A wavelet approach to foveating images. *13th ACM Symposium on Computational Geometry*, pages 397–399, 1997.

[10] Ingrid Daubechies. *Ten Lectures on Wavelets*. SIAM, 1992.

[11] A. Eleftheriadis and A. Jacquin. Automatic face location detection and tracking for model-assisted coding of video teleconferencing sequences at low bitrates. *Signal Processing: Image Communication*, 7(3):231–248, 1995.

[12] R.A. Fisher and H.M. Tong. A full-field-of-view dome visual display for tactical combat training. In *Proc. Image Conference IV*, Phoenix, Arizona, June, 1987.

[13] T. Frajka, P.G. Sherwood, and K. Zeger. Progressive image coding with spatially variable resolution. In *IEEE International Conference on Image Processing*, volume 1, 1997.

[14] G.G. Holmes. The cortical localization of vision. *Br. Med. J*, ii:193–199, 1919.

[15] Philip Kortum and Wilson S. Geisler. Implementation of a foveated image coding system for image bandwidth reduction. In *Human Vision and Electronic Imaging, SPIE Proceedings Vol. 2657*, pages 350–360, 1996.

[16] M. Levoy and R. Whitaker. Gaze-directed volume rendering. *Computer Graphics*, 24(2):217–223, March 1990.

[17] S. Mallat. A theory for multiresolution signal decomposition: the wavelet representation. *IEEE Trans. Pattern Anal. Machine Intell.*, 11:674–692, 1989.

[18] Stephane Mallat. *A Wavelet Tour of Signal Processing.* Academic Press, 1998.

[19] Yves Meyer. *Wavelets and Operators.* Cambridge University Press, Cambridge, 1992.

[20] M. Minkowski. Experimentelle untersuchungen uber die beziehungen der grosshirninde. *Arb. Hirnanat. Inst. Zurich*, 7:259, 1913.

[21] Alireza Moini. Vision chips or seeing silicon. Technical Report, Center for High Performance Integrated Technologies and Systems, The University of Adelaide, March 1997.

[22] F. Panerai, C. Capurro, and G. Sandini. Space variant vision for an active camera mount. In *Proc. SPIE AeroSense95*, 1995.

[23] S. Poliak. The main afferent fibre systems of the cerebral cortex in primates. *Univ. Calif. Publ. Anat.*, 2:107–207, 1932.

[24] E.L. Schwartz. Spatial mapping in primate sensory projection: Analytic structure and relevance to perception. *Biological Cybernetics*, 25:181–194, 1977.

[25] E.L. Schwartz, D.N. Greve, and G. Bonmassar. Space-variant active vision: Definition, overview and examples. *Neural Networks*, 8(7–8):1297–1308, 1995.

[26] Eric L. Schwartz. Topographical mapping in primate visual cortex: history, anatomy, and computation. In D.H. Kelly, editor, *Visual Science and Engineering: models and applications*, chapter 8, pages 293–360. Marcell Dekker, Inc, New York, 1994.

[27] M. Swain and M. Stricker. Promising directions in active vision. *Intern. Journal of Computer Vision*, 11(2):109–126, 1993.

[28] A. Tabernero, J. Portilla, and R. Navarro. Duality between the local spectrum of a signal and its inverse fourier transform, the local signal. Technical Report 53, Instituto de Optica (CSIC), Spain, 1997.

[29] S.A. Talbot and W.H. Marshall. Physiological studies on neural mechanisms of visual localization and discrimination. *Am. J. Ophthalmol*, 24:1255–1263, 1941.

[30] M. Tistarelli and G. Sandini. On the advantages of polar and log-polar mapping for direct estimation of time-to-impact from optical flow. *IEEE Trans. Pattern Anal. Machine Intell.*, 15(4):401–410, 1992.

[31] H.M. Tong and R.A. Fisher. Progress report on an eye-slaved area-of-interest visual display. In *Proc. Image Conference III*, Phoenix, Arizona, May, 1984.

[32] R.S. Wallace, P.-W. Ong, B. Bederson, and E.L. Schwartz. Space variant image processing. *Intl. J. of Computer Vision*, 13(1):71–90, 1994.

A Boundedness of T

Proof.(**of Theorem 1**)

This proof is based on the intuition that foveation is equivalent to a convolution after a change of domain. Let

$$\begin{aligned} f_+(t) &:= f(t)\, 1_{[0,\infty)}(t), \quad \text{and} \\ f_-(t) &:= f(-t)\, 1_{[0,\infty)}(t), \end{aligned}$$

where

$$1_{[0,\infty)}(t) := \begin{cases} 1 & \text{if } t \geq 0 \\ 0 & \text{otherwise.} \end{cases}$$

Let $K_i : L^2(\mathbb{R}^+) \to L^2(\mathbb{R})$, for $i = 1, 2, 3$, and 4 be the operators

$$K_i f(x) = \begin{cases} \int_0^\infty f(t) \frac{1}{x} k_i\left(\frac{t}{x}\right)\, dt & \text{if } x > 0. \\ 0, & \text{otherwise,} \end{cases} \tag{10}$$

where

$$\begin{aligned} k_1(u) &:= g(u-1)\, 1_{[0,\infty)}(u), \\ k_2(u) &:= g(-u-1)\, 1_{[0,\infty)}(u), \\ k_3(u) &:= g(u+1)\, 1_{[0,\infty)}(u), \quad \text{and} \\ k_4(u) &:= g(-u+1)\, 1_{[0,\infty)}(u). \end{aligned}$$

Observe that

$$Tf(x) = \int_0^\infty f(t) \frac{1}{|x|} g\left(\frac{t}{|x|} - \frac{x}{|x|}\right) dt + \int_0^\infty f(-t) \frac{1}{|x|} g\left(\frac{-t}{|x|} - \frac{x}{|x|}\right) dt$$

If $x > 0$, then

$$\begin{aligned} Tf(x) &= \int_0^\infty f(t)\frac{1}{x}g\left(\frac{t}{x}-1\right)\,dt + \int_0^\infty f(-t)\frac{1}{x}g\left(-\frac{t}{x}-1\right)\,dt \\ &= K_1 f_+(x) + K_2 f_-(x); \end{aligned}$$

otherwise,

$$\begin{aligned} Tf(x) &= \int_0^\infty f(t)\frac{1}{-x}g\left(\frac{t}{-x}+1\right)\,dt + \int_0^\infty f(-t)\frac{1}{-x}g\left(-\frac{t}{-x}+1\right)\,dt \\ &= K_3 f_+(-x) + K_4 f_-(-x). \end{aligned}$$

We can combine the above as follow:

$$Tf(x) = K_1 f_+(x) + K_2 f_-(x) + K_3 f_+(-x) + K_4 f_-(-x). \tag{11}$$

Lemma 5 shows that each K_i is bounded.

$$\|K_i\| \le \int_0^\infty |k_i(u)|\,\frac{du}{\sqrt{u}}.$$

Putting the above inequality into (11), we have

$$\begin{aligned} \|Tf\| &\le (\|K_1\| + \|K_2\| + \|K_3\| + \|K_4\|)\,\|f\| \\ \Rightarrow\qquad \|T\| &\le \int_0^\infty |g(u-1)|\frac{du}{\sqrt{u}} + \int_0^\infty |g(-u-1)|\frac{du}{\sqrt{u}} \\ &\quad + \int_0^\infty |g(u+1)|\frac{du}{\sqrt{u}} + \int_0^\infty |g(-u+1)|\frac{du}{\sqrt{u}} \\ &= \int_{-\infty}^\infty |g(u-1)|\frac{du}{\sqrt{|u|}} + \int_{-\infty}^\infty |g(u+1)|\frac{du}{\sqrt{|u|}}. \end{aligned}$$

Q.E.D.

Lemma 5 *Let $L^2(\mathbb{R}^+) := \{f \in L^2(\mathbb{R}) : supp(f) \subseteq [0,\infty)\}$. If $k \in L^1(\mathbb{R}^+)$ is bounded, then the operator K, where*

$$Kf(x) := \int_0^\infty f(t)\frac{1}{x}k\left(\frac{t}{x}\right)\,dt,$$

is bounded and

$$\|K\| \le \int_0^\infty |k(u)|\,\frac{du}{\sqrt{u}} < \infty.$$

Proof. Rewrite K as a convolution after a change of variable (logmap transformation):

$$\begin{aligned}
Kf(x) &= \int_0^\infty f(t)k\left(\frac{t}{x}\right)\frac{dt}{x} \\
Kf(e^y) &= \int_{-\infty}^{\infty} f(e^u)k\left(e^{u-y}\right) e^y de^u \\
& \quad \text{(substituting } t = e^u \text{ and } x = e^y\text{)} \\
&= e^{-y/2}\int_{-\infty}^{\infty} e^{u/2} f\left(e^u\right) e^{(u-y)/2} k\left(e^{u-y}\right) du.
\end{aligned}$$

Let us define the change of variable operator $\Gamma : L^2(\mathbb{R}^+) \to L^2(\mathbb{R})$,

$$\Gamma f(u) := e^{u/2} f\left(e^u\right).$$

Note that

$$Kf(e^y) = e^{-y/2}\left(\Gamma f \star [\Gamma k]^\vee\right)(y),$$

where $^\vee$ is the flip-operator, that is, $h^\vee(x) = h(-x)$. Now, we have

$$\begin{aligned}
e^{y/2}Kf(e^y) &= \left(\Gamma f \star [\Gamma k]^\vee\right)(y) \\
\Rightarrow \Gamma K f(y) &= \left(\Gamma f \star [\Gamma k]^\vee\right)(y). \qquad (12)
\end{aligned}$$

Let $\widetilde{k} := [\Gamma k]^\vee$ and C be the convolution operator defined by:

$$Cg(x) := \left(g \star \widetilde{k}\right)(x).$$

Inserting into (12) gives

$$\begin{aligned}
\Gamma K f(y) &= C\Gamma f(y) \\
\Rightarrow K &= \Gamma^{-1} C \Gamma.
\end{aligned}$$

Note that Γ is a unitary operator, thus we have

$$\|K\| = \|C\|.$$

Since C is a convolution with $\widetilde{k}$,

$$\begin{aligned}\|C\| &\leq \int_{-\infty}^{\infty} \left|\widetilde{k}(u)\right| du \\ &= \int_{-\infty}^{\infty} e^{u/2} \left|k(e^u)\right| du \\ &= \int_0^{\infty} |k(x)| \frac{dx}{\sqrt{x}}.\end{aligned}$$

Hence

$$\|K\| \leq \int_0^{\infty} |k(x)| \frac{dx}{\sqrt{x}} \leq 2\|K\|_\infty + \|K\|_1 < \infty.$$

Q.E.D.

B Decay in the kernel

To prove Theorems 3 and 4, we use the following lemma [19] which relates the magnitude of $|\langle f, \psi_{j,n}\rangle|$ with the local regularity of f and the scale j. The local regularity of a function is measured by its Lipschitz regularity.

Definition

1. *A function f is pointwise Lipschitz $\delta \geq 0$ at v, if there exist $Q > 0$, and a polynomial p_v of degree $m = \lfloor \delta \rfloor$ such that for all $t \in \mathbb{R}$,*

$$|f(t) - p_v(t)| \leq Q|t - v|^\delta. \tag{13}$$

2. *A function f is uniformly Lipschitz δ over $[a, b]$ if it satisfies (13) at $v \in [a, b]$, with a constant Q that is independent of v.*

Lemma 6 *Suppose ψ has q vanishing moments, ψ is C^q and has compact support, and f is uniformly Lipschitz $\delta < q$ over an interval $[a, b]$, then there exist $B > 0$ such that for all $\psi_{j,n}$,*

$$|\langle f, \psi_{j,n}\rangle| \leq B2^{(\delta+1/2)j}.$$

Proof. **(of Theorem 3)** Parts (a) and (b) can be easily verified using the fact that both g and ψ have compact support. For (c), we will only show $|\theta_{j,m,k,n}| \leq E2^{(k-j)(p+1/2)}$. Since either $|n| > 2\alpha^{-1}$ or $|m| > 2\alpha^{-1}$, if $nm < 0$ then $\theta_{0,m,k,n} = 0$. If $n > 0$ and $m > 0$, then

$$\theta_{0,m,k,n} = \int_0^\infty \int_0^\infty \psi_{k,n}(x)\psi_{0,m}(t)(\alpha x)^{-1} g\left(\frac{t-x}{\alpha x}\right)\, dt\, dx.$$

Otherwise, if $n < 0$ and $m < 0$, then

$$\theta_{0,m,k,n} = \int_{-\infty}^0 \int_{-\infty}^0 \psi_{k,n}(x)\psi_{0,m}(t)(-\alpha x)^{-1} g\left(\frac{t-x}{-\alpha x}\right)\, dt\, dx.$$

We only consider the first case ($n > 0$ and $m > 0$) since the second case is similar.

$$\begin{aligned}\theta_{0,m,k,n} \quad &= \int_0^\infty \int_0^\infty \psi_{k,n}(x)\psi_{0,m}(t)(\alpha x)^{-1} g\left(\frac{t-x}{\alpha x}\right)\, dt\, dx, \\ &= \int_0^\infty \psi_{k,n}(x) \int_0^\infty \psi_{0,m}(t'x)\alpha^{-1} g\left(\frac{t'-1}{\alpha}\right)\, dt'\, dx. \qquad (14) \\ &\quad \text{(by substituting } t' = tx^{-1}\text{)}\end{aligned}$$

If $n > 2\alpha^{-1}$, then $\psi_{k,n}(x) = 0$ for $x < c$, where c is some positive constant. Using this fact, (14) can be rewritten as

$$\int_{-\infty}^\infty \psi_{k,n}(x) \int_0^\infty \psi_{0,m}(t'x)\alpha^{-1} g\left(\frac{t'-1}{\alpha}\right)\, dt'\, dx.$$

Otherwise, we have $m > 2\alpha^{-1}$. Since ψ has compact support, $\psi_{0,m}(t'x) = 0$ whenever t' and x have different sign. Therefore, (14) can again be rewritten as the above.

Since $\mathtt{supp}(g) \subseteq [-\alpha^{-1}, \alpha^{-1}]$, we have

$$\mathtt{supp}(g(\alpha^{-1}(\cdot - 1))) \subseteq [0, 2],$$

$$\begin{aligned}\theta_{0,m,k,n} \quad &= \quad \int_0^2 \alpha^{-1} g\left(\frac{t-1}{\alpha}\right) \int_{-\infty}^\infty \psi_{k,n}(x)\psi_{0,m}(tx)\, dx\, dt \\ &= \quad \int_0^2 \alpha^{-1} t^p g\left(\frac{t-1}{\alpha}\right) \int_{-\infty}^\infty \psi_{k,n}(x)\left(t^{-p}\psi_{0,m}(tx)\right)\, dx\, dt.\end{aligned}$$

Since $\psi_{0,m}$ is C^p, then so is the function $t^{-p}\psi_{0,m}(\cdot t)$. Together with Lemma 6,

$$\left|\int_{-\infty}^{\infty} \psi_{k,n}(x)t^{-p}\psi_{0,m}(tx))\,dx\right| \leq E_1 2^{k(p+1/2)},$$

for some constant E_1. Therefore

$$|\theta_{0,m,k,n}| \leq \max_{0\leq t\leq 2}\left\{\left|\alpha^{-1}t^p g\left(\frac{t-1}{a}\right)\right|\right\}\cdot\int_0^2 E_1 2^{k(p+1/2)}\,dt = E_2 2^{k(p+1/2)}.$$

By self-similarity, we have the result.

Q.E.D.

Proof.(**of Theorem 4**)

We will only show $|\theta_{j,m,k,n}| \leq F\ 2^{(j-k)(\rho+1/2)}|n|^{-(\rho+1)}$. The other case is similar.

Rewriting $\theta_{j,m,0,n}$, we have

$$\theta_{j,m,0,n} = \int_{-\infty}^{\infty} \psi_{0,n}(x)|\alpha x|^{-(\rho+1)}\int_{-\infty}^{\infty}\psi_{j,m}(t)\left(|\alpha x|^{\rho} g\left(\frac{t}{\alpha x}-1\right)\right)\,dt\,dx.$$

Since g is uniformly Lipschitz ρ, then so is $(\alpha x)^\rho g(\cdot/(\alpha x)-1)$. Together with Lemma 6,

$$\begin{aligned}|\theta_{j,m,0,n}| &\leq \int_{-\infty}^{\infty}\left|\psi_{0,n}(x)(\alpha x)^{-(\rho+1)}F_1 2^{j(\rho+1/2)}\right|\,dx\\ &= F_1 2^{j(\rho+1/2)}\int_{n-\alpha^{-1}}^{n+\alpha^{-1}}\psi_{0,n}|\alpha x|^{-(\rho+1)}\,dx.\end{aligned}$$

Since $|n| > 2\alpha^{-1}$,

$$\begin{aligned}|\theta_{j,m,0,n}| &\leq F_1 2^{j(\rho+1/2)}(\alpha|n-\alpha^{-1}|)^{-(\rho+1)}\int_{-\infty}^{\infty}|\psi_{0,n}(x)|\,dx\\ &\leq F_2 2^{j(\rho+1/2)}|n|^{-(\rho+1)}.\end{aligned}$$

By self-similarity, we have

$$|\theta_{j,m,k,n}| \leq F_2^{(j-k)(\rho+1/2)}|n|^{-(\rho+1)}.$$

Q.E.D.